RSC Advances

ROYAL SOCIETY OF CHEMISTRY

www.rsc.org/advances

Vacancy mediated ionic conduction in Dy substituted nano ceria: A structure-property correlation study

Sk Anirban[a,b], Tanmoy Paul[a] and Abhigyan Dutta[a,*]

[a]Department of Physics, The University of Burdwan, Burdwan-713104, India

[b] Department of Physics, Govt. General Degree College, Singur, Hooghly-712409, India

Abstract

The oxygen vacancy evolution and ion dynamics in the Dy doped nanoceria has been investigated with microstructural, optical and ionic conductivity study. The influence of Dy^{3+} ions on the microstructure, optical and ionic conductivity properties of these nanoparticles have been studied using X-ray diffraction, HR-TEM, EDAX, UV-vis, Raman and impedance spectroscopy. From Rietveld refinement of the XRD profiles, it has been found that, the oxygen vacancy, lattice parameter and Ce-O bond length increases with the Dy^{3+} ions concentration. The Rietveld analysis together with HR-TEM confirms the cubic fluorite structure with space group $Fm\bar{3}m$ of all the samples. The EDAX spectra represent a good stoichiometry of different atoms in the samples. The direct band gap, calculated from UV-vis spectra, has shown a red shift with the concentration of Dy^{3+} ions. Raman spectroscopy study of the samples gave insight to vibrational properties and pointed to the fact that, the content of oxygen vacancy increased significantly with the doping concentration. The number of oxygen vacancy and their interaction with dopant cations strongly influence the electrical properties of Dy doped ceria.

Keywords: Ceria, X-ray diffraction (XRD); Microstructures; Optical properties; Ionic conductivity

***Author for correspondence: A. Dutta**

Address: Department of Physics, The University of Burdwan, Golapbag, Burdwan-713104, INDIA email: adutta@phys.buruniv.ac.in **; Telephone: +913422657800; Fax: +91342 2634015**

1. Introduction:

Ionic conductivity of ceria based solid solutions has been reported to be an order magnitude greater than that of yttrium-stabilized zirconia (YSZ) when it is in nanocrystalline form [1]. Ceria based nanomaterials have also found their applications as catalytic support in automotive exhaust systems [2]. Rare earths are praised as the treasury of materials due to their special optical, electrical and magnetic properties which are attributed to their particular electron configuration [3]. When ceria is doped with rare earths, then substitution of Ce^{4+} in ceria by these trivalent cations distorts the lattice structure and generates oxygen vacancies [4], which permits high oxygen ion conduction. The oxygen vacancy concentration of CeO_2 can be varied by varying dopant concentration [5]. Rare earth doped ceria is also a good candidate as wave length converter of near UV photons to IR photons [6]. A comprehensive knowledge of the crystal structure and a better understanding of the mechanism of ionic conduction are therefore required to develop a better electrolyte material. Hence, to use rare earth doped ceria as electrolyte materials, many researchers have studied the crystal structure, ordering of oxygen vacancies and diffusion path of these ionic conductors [7-10]. The movement of these oxygen vacancies is influenced by their interaction with dopant cations. A relatively small concentration of point defects may affect the physical properties of these materials in very significant ways [11]. Raman spectroscopy is an

essential tool to investigate this type of local structural distortion [12]. The main difficulty for application of rare earth doped ceria in SOFC electrolyte is the creation of both electronic and ionic charge carriers at low oxygen partial pressures. The ionic conduction in rare earth doped ceria is dominated by the association between trivalent cations and oxygen vacancies. Among various rare earth doped ceria materials, ceria doped with Sm^{3+} and Gd^{3+} shows higher ionic conductivity because of their optimum radius and thereby a smaller association enthalpy [13,14]. Recent studies [15] has also pointed out that Dy doped ceria may be a promising solid electrolyte material for applications in low temperature SOFCs.

In our present work, Dy doped $Ce_{1-x}Dy_xO_{2-\delta}$ ($0.0 \leq x \leq 0.5$) nanoparticles were prepared by using the citrate auto-ignition method. The detailed microstructure and the optical properties of these nanoparticles were investigated. The effect of dysprosium doping on the evolution of oxygen vacancies with respect to microstructure, optical properties and the dependence of electrical conductivity on doping concentration and oxygen vacancies are discussed and correlated.

2. Materials and Methods:

The Dy doped ceria nanomaterials $Ce_{1-x}Dy_xO_{2-\delta}$ ($0.0 \leq x \leq 0.5$) were prepared by using low temperature citrate auto-ignition method. $Ce(NO_3)_3$, $6H_2O$ (99.9%) and Dy_2O_3 (99.9%) were used as starting materials. The process of sample preparation has been described in our previous work [16]. The as prepared powdered samples were annealed at 400^{o}C for 2 h then again sintered at 600^{o}C for 6 h. During annealing/sintering the rise in temperature was in rate 5^{o}C/min. and then materials were cooled down to room temperature by normal furnace cooling. To identify the crystal structure and phase purity of the samples, X-Ray diffraction profiles were recorded with a powder X-ray diffractometer (BRUKER, Model D8 Advance-AXS) using CuK_α radiation[

λ=1.5406 Å] from 2θ = 20° to 90° with step size 0.05°. The morphology of the sintered samples was examined using scanning electron microscopy (SEM) (Carl Zeiss SMT Ltd. SUPRA™ 40). The microstructural analysis at high magnification were performed by placing the particles in a formvar-carbon coated 300 mesh copper grid with the help of transmission electron microscope (JEOL, Model JEM- 2010) operated at 200 kV. The TEM micrographs were further analyzed using Gatan microscopy suite. The compositions of the samples were evaluated from energy dispersive X-ray analysis (Hitachi S-3500). Ultraviolet–visible (UV–vis) absorption spectra were taken at room temperature in the wavelength range 200–1100 nm using Shimadzu spectro-photometer (Model-1800). Raman spectra of the materials were recorded at room temperature in a Triple Raman Spectrometer (Jobin-Yvon Horiba T64000) equipped with a TE cooled charge coupled-device detector and an Olympus microscope using He-Ne laser at 632.817 nm line as the excitation source in the wave number range 200-800 cm^{-1}.For electrical measurements, cylindrical pellets were prepared from sintered powder by uniaxial pressing in a 10 mm diameter stainless steel die. The pellets were covered on both sides with conductive graphite paste to make the electrodes. The electrical measurements were performed using two probe methods in air. A LCR meter (HIOKI, Model 3532-50) interfaced with PC was used to collect the electrical data in the frequency range 42Hz-5MHz and in the temperature range 250-550°C.

3. Results and discussion:

3.1. X-Ray diffraction analysis and Rietveld refinement:

Fig. 1(a) shows the XRD pattern of the $Ce_{1-x}Dy_xO_{2-\delta}$ (x=0.00 – 0.50) samples. It may be found that, when ceria is doped with Dy, there is no noticeable change in the diffraction pattern i.e. any evaluation of additional peak due to Dy is absent. This ensures the complete dissolution of Dy

into the ceria lattice. The observed peaks in the XRD pattern were well indexed and consistent with the reference data [JCPDS file: 34-03940]. The observed Bragg reflection peaks confirmed the cubic fluorite structure of the samples. We have plotted the maximum intensity peak (111) with the concentration of Dy in Fig. 1(b). It can be seen from Fig. 1(b) that the peak shifts towards the lower angle side with doping concentration x. This shift of (111) peak clearly indicates the lattice expansion with Dy content in the ceria lattice.

To obtain the microstructural information of the samples, we have performed the Rietveld analysis of the XRD data using MAUD 2.33 software, which is specially designed to refine simultaneously both the structural and microstructural parameters through a least square method. Fig. 1(c) and (d) show the refined XRD pattern obtained from Rietveld analysis for the samples x = 0.20 and x = 0.50 respectively. The shape of the diffraction profile is fitted with a pseudo-Voigt function (it is described by Gaussian + Lorentzian functions with refinable degree of mixing) with asymmetry because it takes care of individual for the both particle size and strain broadening of the experimental data [17]. The angular dependence of the peak full width at half maximum (FWHM) is described by Caglioti's formula. The background of each XRD profile is fitted using a polynomial of degree 5. The difference between observed and simulated diffraction pattern was minimized using Marguardt least-squares procedure. This minimization was carried out by using the reliability index parameter such as weighted residual error (R_{wp}), expected error (R_{exp}) and goodness of fit (GoF) [18-20]. These parameters are defined as:

$$R_{wp}=\sqrt{\frac{\sum w_n(Y_{0,n}-Y_{c,n})^2}{\sum w_n(Y_{0,n}-Bkg_n)^2}} \quad (1)$$

$$G.O.F=\sqrt{\frac{\sum w_n(Y_{0,n}-Y_{c,n})^2}{N-P}} \quad (2)$$

where $Y_{o,n}$ and $Y_{c,n}$ are respectively the observed and calculated data at point n, Bkg_n, is the background at data point n, N is the number of data points, P is the number of parameters and

$w_n$is the weighting factor given to data point n. In counting statistics, this last factor is given by $w_n=1/\sigma(Y_{o,n})^2$, where $\sigma(Y_{o,n})$ is the error in $Y_{o,n}$. Both R_{wp} and GoFare good global indicators of the refinement process, since the numerators of these factors contain the residual function which is being minimized. A rather good refinement is represented by low values of these parameters: R_{wp} around 0.10 for XRD in a conventional diffractometer, and GoF around 1 [21]. In all refinements GoF is between 1.1 and 1.2 which indicates the goodness of refinement. Different Reitveld parameters like R_{exp}, R_{wp} and GoF for each XRD profile are enlisted in Table 1. We have evaluated the effective particle size (D) and r.m.s. strain ($<\varepsilon^2>^{1/2}$) using the Popa model [22]. Other structural parameters as lattice parameter, Ce-O bond length, atomic position and occupancies were calculated which are given in Table 1.

The Rietveld analysis indicated the cubic fluorite structure of each sample with space group $Fm\bar{3}m$. In this structure cerium ions occupy the vertices and face of cubic unit cell. Each cerium ion (Ce^{4+}) is co-ordinated with eight oxygen ions (O^{2-}) arranged in perfect cube while each oxygen ion is surrounded by four cerium ions in tetrahedral arrangement. This structure is often described as cubic closed packing of cerium ions with oxygen ions occupying all tetrahedral holes [23]. The crystal structure of pure ceria is shown in Fig. 2(a). All the cerium ions (Ce^{4+}) are situated at the 4a site with the atomic co-ordinate (0,0,0) and oxygen ions (O^{2-}) are at the site 8c corresponding to the (1/4, 1/4, 1/4) position. All the ions positions are fixed during the whole refinement process. Generally the fluorite structured ceria, when doped with a trivalent cation like Dy^{3+}, one oxygen vacancy is formed for every two trivalent cations for charge neutrality and represented by the Kröger-Vink notation:

$$Dy_2O_3 + 2CeO_2 \rightarrow 2Dy'_{Ce} + 3O_o^x + V_o^{\bullet\bullet} \quad (3)$$

Here Dy'_{Ce} indicates one Ce^{4+} site occupied by Dy^{3+} ion and $V_o^{\bullet\bullet}$ represents the oxygen vacancy. The defect structure of the doped ceria is shown in Fig. 2(b). Here the occupancy of Ce^{4+} ions in the 4a site and O^{2-} ions in 8c site of undoped ceria is 1 (Table 1). In doped ceria, the occupancy of Ce^{4+} ions decreases with the doping concentration and the occupancy of dopant ions (Dy^{3+}) in 4a site increases. The occupancy of O^{-2} ions at 8c side decreases with doping concentration of Dy^{3+} ions, which indicates more number of oxygen vacancies. The formation of these oxygen vacancies were confirmed in earlier studies [24-27]. Fig. 3 shows the variation of lattice parameter of $Ce_{1-x}Dy_xO_{2-\delta}$ (x=0.00 – 0.50) samples as a function of total dopant concentration (x). It can be seen that, the lattice parameter increases with dopant concentration which is due to the fact that, ionic radius of Dy^{3+} (1.027Å) is greater than the ionic radius of Ce^{4+} (0.97Å). It can be seen from Fig. 3 that, for $Ce_{1-x}Dy_xO_{2-\delta}$ system, the lattice parameter increases linearly with the increase of Dy^{3+} concentration upto x = 0.25 following Vegard's law [28]. After x = 0.25 lattice parameter of the system $Ce_{1-x}Dy_xO_{2-\delta}$ also increases linearly but the rate of increase is different. Using a least-square fitting algorithm a linear relationship was obtained between lattice parameter (a) and dopant concentration (x). These can be represented as,

$$a\ (x, 0 \le x \le 0.25) = 5.39771 + 0.04369x \quad (4)$$

and

$$a\ (x, 0.3 \le x \le 0.5) = 5.40451 + 0.01847x \quad (5)$$

Similar results were also found earlier for $Ce_{1-x}Gd_xO_{2-\delta}$ ($0.05 \le x \le 0.4$) system [29]. In the present study, the slower increase of lattice parameter at higher concentration ($x > 0.25$) can be attributed to the effect of the interaction between dopant cations and oxygen vacancies which tend to contract the unit cell [30]. As the oxygen vacancy increases with doping concentration x, at higher doping concentration number of oxygen vacancies are much greater. So, the interaction between oxygen vacancies and dopant ions is greater at higher concentration. At higher doping

concentration oxygen vacancies and defect associations appearing in the solid solutions are surely to have different interactions with the network ions and the oxygen vacancy is believed to produce a lattice contraction than the defect association [31]. The r.m.s. strain for the sample $Ce_{0.8}Dy_{0.2}O_{2-\delta}$ shows a minimum value 1.25×10^{-5}. The Ce-O bond length of the system was also evaluated from Rietveld analysis and was found to increase with x i.e. the change in lattice parameter is also followed by the Ce-O bond length change. During the formation of rare earth doped ceria solid solutions, several defect reactions can be created. Among them oxygen vacancy model is very much important which is represented by the Kröger-Vink notation as given earlier. With the help of this oxygen vacancy model of doped ceria we can find out the density of the system $Ce_{1-x}Dy_xO_{2-\delta}$ (x=0.00 – 0.50) using the following equation:

$$\rho_v = \frac{4xM_{Dy} + 4(1-x)M_{Dy} + 4(2-\frac{x}{2})M_O}{N_A a^3} \quad (6)$$

Where M_{Dy}, M_{Dy} and M_O are the atomic weight of Dy, Ce and Oxygen repectively; N_A is Avogadro no. and a is lattice parameter. The value of density is given in the Table 1 and found to increase with doping concentration as the atomic weight of Dy (162.5) is greater than Ce (140.11).

3.2. Energy Dispersive X-ray Analysis:

The composition of the obtained system was analyzed by means of energy dispersive X-ray analysis (EDAX). Figs. 4(a-d) shows EDAX spectrum for the compositions x = 0.00, x = 0.10, x = 0.20 and x = 0.50 respectively. The presence of major chemical elements namely Cerium, Dysprosium and Oxygen in prepared samples was confirmed from this analysis. The percentage of Dy/Ce values are given in the inset of Figs. 4(a-d). The doped ceria did not deviate from their initial stoichiometry and matched well with the initial degree of Dy substitution The EDAX spectrum clearly shows that oxygen content in the system $Ce_{1-x}Dy_xO_{2-\delta}$ decreases with the

doping concentration i.e. the oxygen vacancies increase with doping concentration. This result is in good agreement with the Rietveld analysis results discussed earlier.

3.3. Transmission Electron Microscopy (TEM) Study:

The nano structure of the samples was further characterized by using transmission electron microscopy. The nano flakes for the sample x = 0.2 are distributed uniformly as observed in bright field TEM image of Fig. 5(a). All the samples show similar nano structure with negligible size variation with composition. The crystallite size distribution for the sample x = 0.2 is shown in the inset of Fig. 5(a). It can be inferred that, the average crystallite size is ~ 16.84 nm indicating the sample preparation is correct to produce such kind of nanostructure. In Fig. 5(b), the lattice fringe pattern is shown for the composition x = 0.2. The fast Fourier transform (FFT) of the embraced zone is shown in the inset of Fig. 5(b). At least three different pairs of bright spots are found and these spots are identified as reflections from (111), (002) and (11-1) lattice planes as shown in the inset of Fig. 5(b). The sharp and bright spots further confirmed the cubic symmetry and well crystallinity of the sample. Using SAED studies D.R. Ou et al. have shown an increase in local ordering of oxygen vacancies with the increase of doping concentration in lanthanide doped ceria [32]. In Fig. 5(c) the simulated lattice pattern is also shown with prominent lattice planes orientated along (111) direction. It can be inferred that, the lattice fringe in Fig. 5(c) consists of (111), (002) and (11-1) planes as previously suggested by FFT pattern. To get more information we have analyzed the atomic model using the XRD refinement results. Fig. 5(c) contains all of these lattice planes with viewing direction along [-110] as suggested by the atomic model in Fig. 5(d). It can be noted that Dy^{3+} is partially occupying Ce^{4+} site so they cannot be isolated but the position of cation (Ce^{4+}/Dy^{3+}) is detectable as observed in Figs. 5(c) and (d).

3.4. UV-vis spectroscopy:

Fig. 6(a) shows the UV-VIS absorption spectra recorded for pure and doped ceria. It can be seen that, there is a strong absorption band below 400 nm in the spectrum for all the samples which is due the charge transfer from $O^{-2}(2p)$ to $Ce^{4+}(4f)$ orbitals in CeO_2 [33]. But there is no absorption in the visible region. The optical band gap values for $Ce_{1-x}Dy_xO_{2-\delta}$ (x=0.00 – 0.50) system can be estimated from the absorption spectra data following Tauc's rule [34]:

$$\alpha h\nu = A(h\nu - E_g)^n \quad (7)$$

where α is the absorption co-efficient hν is the photon energy, E_g is the band gap energy, A is a constant and n can take values 1/3, 1/2 , 2, 3 for the direct forbidden, direct allowed, indirect allowed, indirect forbidden transition respectively. The band gap corresponding to direct transition was obtained by extrapolating the linear portions of $(\alpha h\nu)^2$ versus hν curves to $(\alpha h\nu)^2$ equal to zero. A plot of $(\alpha h\nu)^2$ as a function of photon energy hν for the sample $Ce_{0.75}Dy_{0.25}O_{2-\delta}$ is shown in Fig. 6(b). The calculated values of E_g for all the samples are given in Table 2. Undoped ceria shows the highest band gap value of 2.750 eV and for Dy^{3+} doped ceria the values of band gap decreases with dopant concentration x. Thus the absorption spectra of Dy^{3+} doped ceria nanocrystals exhibits a red shift compared to pure ceria. In CeO_2, all valance Ce states including 4*f* states are empty and the system is wide gap insulator with a measured fundamental band gap of 6.0 eV between the valance and conduction band which is formed predominantly by O^{-2} (2*p*) to Ce^{4+} (5*d*) states respectively [35]. The vacant 4*f* states lie in the gap. But in our present study, the band gap values of CeO_2 is quite lower than 6.0 eV. This is because, the presence of small amount of Ce^{3+} at the surface of CeO_2 [36] and one electron per Ce atom populates a Ce 4*f* state resulting in decrease in band gap values of ceria. The co-existance of a small amount of Ce^{3+} ions was also confirmed by using XPS analysis [37]. The red shift of direct band gap with x

can be explained in several ways. Firstly, when Dy^{3+} ions are incorporated into the ceria lattice, the valancy changes from Ce^{4+} to Ce^{3+} ions decreases due to the replacement of Ce^{3+} ions by trivalent Dy^{3+} ions as confirmed by several authors using XPS [38-40]. The substitution of Ce^{3+} ion with Dy^{3+} ion increases with doping concentration and such a substitution increases the oxygen vacancy concentration due to charge compensation mechanism as discussed earlier. Secondly, the red shift may due to the presence of the oxygen defect levels present in between O2*p* and Ce4*f* levels that capture the excited electrons and decrease the effective band gap [41]. Lastly, the doping of Dy ions creates ground and excited *f*-energy states in the mid band gap of ceria. These energy states of Dy take up many of the excited electrons coming from O2*p* level [11]. This ultimately leads to effective reduction in band gad i.e. read shift.

3.5. Raman spectroscopy:

Raman spectra of sintered samples $Ce_{1-x}Dy_xO_{2-\delta}$ (x = 0.0-0.5) are shown in Fig. 7. These spectra exhibit a high intense Raman band centered at 462 cm^{-1} to 484 cm^{-1} as listed in Table 3. These bands were attributed to the Raman-active vibrational mode F_{2g} of fluorite-type structure that can be viewed as a symmetrical stretching vibration of oxygen atoms around Ce^{3+} ions [42] and are sensitive to the crystalline symmetry [43]. Table 3 also reveals that, F_{2g} mode shifts towards the higher wave number with the concentration of Dy^{3+}cations (i.e. with x). This shift is due to the increase of oxygen vacancy i.e. decrease of the amount of oxygen ions bound to Ce or Dy ions [44]. Therefore, number of oxygen vacancies increases in the system $Ce_{1-x}Dy_xO_{2-\delta}$ (x = 0.0-0.5) with x and this is well in agreement with the Rietveld analysis result. A second order Raman band below 400 cm^{-1} and above 500 cm^{-1} was observed which is due to the extrinsic oxygen vacancies introduced into the ceria when Ce^{4+} ions are replaced by the Dy^{3+} ions. These Raman bands are also due to defect spaces like $M_4O_v$and O_6O_v type complex (M = metal ions and O_v

oxygen vacancy) where M_4O_v type complex consists of an oxygen vacancy surrounded by four nearest neighbor metal ions and O_6O_v type complex consists of an oxygen vacancy surrounded by six next nearest neighbor oxygen ions. These second order Raman bands below 400 cm^{-1} were also observed in earlier studies [45]. The relative intensity of these bands also increases with the doping concentration of Dy^{3+}cations. For pure ceria, only an intense band centered at 462 cm^{-1} is observed and no other bands were observed which signifies that, there is apparently no extrinsic oxygen vacancy. As shown in the Fig. 7, for all the doped samples, there is a D band above 500 cm^{-1} which splits into D_1 and D_2 bands for the samples x = 0.1-0.4. The D_1 and D_2 bands were merged into a broad single band for the sample x = 0.5. The center of D_1 and D_2 bands shifts towards the higher wave number side with the concentration of Dy^{3+}cations. These disordered D_1 and D_2 bands were used as a powerful tool to investigate the defect association formed to decrease the total lattice energy in ceria based materials [46]. Hence, the D_2 bands from 597 cm^{-1} to 610 cm^{-1} are attributed to defect spaces with O_h symmetry which include a Dy^{3+} atom in 8-fold co-ordination of O^{2-} but does not contain any O^{2-} vacancy. The D_1bands from 552 cm^{-1} to 576 cm^{-1} were assigned to defect spaces with symmetry other than O_h symmetry that include O^{2-} vacancy in $(2Dy'_{Ce}\text{-}V_O^{\bullet\bullet})^{\times}$ and $(Dy'_{Ce}\text{-}V_0^{\bullet\bullet})^{\bullet}$ complexes. Both the D_1 and D_2 bands shifts towards to the higher wave number side with the concentration of Dy^{3+} ions and the shift of D_1 is assigned to the increase of $(2Dy'_{Ce}\text{-}V_O^{\bullet\bullet})^{\times}$ complex compared to that of the $(Dy'_{Ce}\text{-}V_0^{\bullet\bullet})^{\bullet}$ complex. The ratio of intensities of different bands is listed in Table 3. The ratio of $I_{F_{2g}}/I_{D_1}$ and $I_{F_{2g}}/I_{D_2}$ decreases with the increase of x which is related to the degree of defect sites on CeO_2. This also indicates higher number of oxygen vacancies with higher doping concentration [47]. According to Nakajima et. al. [48], low ratio of I_{D_1}/I_{D_2} indicates that Ce^{3+} ions preferably locate in a $Ce^{3+}O_8$ type complex and higher value of this ratio indicates an increase of concentration of the O^{2-} vacancies

amalgamated defects with $Dy^{3+}O_8$ type complex. S. F. Wang et. al [49] and Z. D. Dohčević-Mitrović et al. [50] have also showed the increase of oxygen vacancies with doping concentration in the rare earth doped ceria solid solution using Raman spectroscopy. The shift of Raman bands and change in intensity ratio with doping concentration also confirms the formation of solid solutions in our present study by citrate auto-ignition method.

3.6. Electrical conductivity:

Fig. 8(a) shows the variation of real part $\sigma'(\omega)$ of complex conductivity as a function of frequency at a temperature 525°C of the system $Ce_{1-x}Dy_xO_{2-\delta}$ ($0.0 \leq x \leq 0.5$). This figure reveals that conductivity spectra of this system consists of two parts viz. a frequency independent part in the low frequency region which corresponds to dc conductivity caused by the random hopping of the ions and frequency dependent part at high frequency region which corresponds to ac caused by the correlated forward backward hopping motion of the charge carriers among the localized sites [51]. Therefore the conductivity spectra can be well described by the following equation:

$$\sigma' = \sigma_{dc} + \sigma_{ac} \quad (8)$$

This spectrum also shows a similar nature of all the compositions. The Random free-energy Barrier Model (RBM) proposed by Dyre [52], describes the frequency dependent conductivity, over a wide range of frequencies, in disordered solids at constant temperature. This model is based on the ascertainment that dc conductivity is more thermally activated than ac conductivity. We used RBM to evaluate the dc conductivity or the total conductivity. According to RBM, the complex conductivity $\sigma^*(\omega)$ is given by

$$\sigma^*(\omega) = \sigma(0)\frac{i\omega\tau_e}{\ln(1+i\omega\tau_e)} \quad (9)$$

, where $\sigma(0)$ is the dc conductivity and $\omega_e = \frac{1}{\tau_e}$ is the attempt frequency to overcome the highest free energy barrier. The real part of $\sigma^*(\omega)$ has been used to fit the conductivity spectra as shown in Fig. 8(a). The variation of $\sigma(0)$ with the doping concentration of Dy^{3+} for different temperatures is shown in Fig. 8(b). This figure reveals that, the dc conductivity increases with doping concentration and shows a maximum value for x = 0.20 and further increase of doping concentration decreases the conductivity. The oxygen vacancies inside the grain and grain boundary control the whole conduction process. This variation may be due to the number of oxygen vacancies present in the system and the interaction between oxygen vacancies and dopant cations. As discussed earlier, oxygen vacancies increases with doping concentration, so, it is expected to increase the conductivity with doping concentration. At higher doping concentration number of oxygen vacancies will be more, so there may be strong interaction between these vacancies with Dy^{3+} ions. Therefore, the motion of free oxygen vacancies at higher doping concentration should be limited and conductivity decreases. Fig. 8(c) shows the temperature dependence of dc conductivity $\sigma(0)$, which obeys the Arrhenius equation given by

$$\sigma(0) = \frac{\sigma_0}{T} e^{-E_a/K_B T} \qquad (10)$$

Where σ_0 is the pre-exponential factor being a constant in a certain temperature range, K_B is the Boltzman's constant, T is the absolute temperature and E_a is the activation energy for dc conduction. E_a can be calculated easily from the slope of Arrhenius plot. It is observed in Fig. 8(c) that the dc conductivity increases with temperature which indicates that, oxygen ion conduction in these compositions are thermally activated process. The activation energies for dc conduction are listed in Table 4. The activation energy shows a minimum value for the sample x = 0.20 which shows the maximum conductivity. In another study of S. Kuharuangrong [53] the

activation energy for x = 0.10, x = 0.20 and x = 0.30 was reported as 1.06 eV, 1.11eV and 1.15 eV respectively and the composition x = 0.30 shows the highest conductivity among the all others compositions. These activation energy values are very close to our system. Again according to S.Acharya[15], the composition x = 0.15 shows a lowest activation energy (0.86 eV) and highest conductivity (7.42×10^{-2} S/cm). A.K. Baral et al.[27] had reported activation energy and conductivity at 550^{o}C for the composition x = 0.20 in their study as 1.16 eV and 1.36×10^{-4} S/cm respectively. But in our present system the composition x = 0.20 shows lower activation energy and higher conductivity at 550^{o}C (5×10^{-4} S/cm) than the previous study by A.K. Baral et al. Again Y. Wang et al. [54] was reported activation energy and conductivity for the composition x = 0.10 in their study as 0.79 eV and 2×10^{-4} S/cm respectively. Therefore, the conductivity and activation energies are comparable to the previous reported study. The values of activation energy and conductivity of our present study and previous study are also listed in Table 4. The scaling behavior of conductivity spectra shows the effect of temperature on the conduction mechanism. The conductivity spectra of the compositions obey the time-temperature superposition principle (TTSP) i.e. all the conductivity spectra at different temperatures are superimposed on a single master curve. In case of the real part of complex conductivity the TTSP can be represented by the following scaling law [55]

$$\frac{\sigma'(\omega)}{\sigma(o)} = F(\omega\tau_e) \qquad (11)$$

The scaling function F is independent of both the temperature and composition. Fig. 9(a) shows the superposition of all the curves on a master curve for x = 0.20. Similar behavior was also found for other compositions. This behavior simply indicates that, the conduction mechanism (movement of oxygen ions through the crystal lattice as a result of thermally activated hopping

of the oxygen ions moving from a crystal lattice site to another crystal lattice site) does not depend on temperature i.e. the change in temperature only changes the number of charge carriers without changing the conduction mechanism [56]. Fig. 9(b) shows the scaled spectra for different compositions for a particular temperature which shows the superposition of all the curves on a single curve. This indicates the doping concentration independence of the conduction mechanism. More clearly migration of charge carrier in our present system takes place through a simple hopping mechanism. The only likely migration events involve an oxygen ion hopping to a vacancy in a nearest neighbor or a next nearest neighbor site thus exchanging its place with the vacancy. The increase of doping concentration only changes the number of oxygen vacancies but the conduction mechanism as mentioned above remains unchanged.

4. Conclusion:

In summary, Dy doped ceria-based nanoparticles were obtained by citrate auto-ignition method. A good stoichiometry of the atoms in the obtained samples was confirmed by EDAX. Rietveld analysis of the XRD data and HRTEM of the sintered samples confirmed the well crystalline and single phase cubic fluorite structure with space group $Fm\bar{3}m$. The variation of lattice parameter with doping concentration tends to saturate at higher doping concentration due to interaction between oxygen vacancies and cations. The UV-VIS absorption measurements showed a red shift in the absorption peak positions with the concentration of Dy^{3+} ions and were explained in terms of the compensation of Ce^{3+} ions, generation of oxygen vacancies and creation of *f*-energy states. The Rietveld analysis and the shift of different Raman bands confirmed the increase of oxygen vacancies with doping concentration. The Raman spectra also reveal the presence of different defect spaces like M_4O_v, O_6O_v, $Ce^{3+}O_8$ and $Dy^{3+}O_8$ type complex

including oxygen vacancy. The dc conductivity and activation energy vary with doping concentration due to oxygen vacancies and interaction between vacancies and dopant cations.

5. Acknowledgements:

One of the authors (AD) thankfully acknowledges the financial assistance from Department of Science and Technology (Govt. of India) (Grant no: SR/FTP/PS-141-2010). The authors (SA and AD) also acknowledge the instrumental support from DST (Govt. of India) under departmental FIST programme (Grant no: SR/FST/PS-II-001/2011) and University Grants Commission (UGC) for departmental CAS scheme.

6. Reference:

1 B. C. H. Steele, *Solid State Ionics*, 2000, **129**, 95-110.

2 E. Bekyarova, P. Fornasiero, J. Kaspar, M. Graziani, *Catal. Today*, 1998,**45**, 179-183.

3 L. Zhaogang, L. Mei, H. Yanhong, W. Mitang, S. Zhenxue, *J. Rare Earths*, 2008, **26**, 158-162.

4 Zhi-Peng Li, T. Mori, F. Ye, D. Ou, J. Zou, J. Drennam, *J. Chem. Phys*., 2011,**134**, 224708.

5 B. Choudhury, A. Choudhury, *Curr. App. Phys.*, 2013,**13**, 217-223.

6 J. Ueda, S. Tanabe, *J. Appl. Phys*., 2011, **110**, 073104.

7 M. Yashima, S. Kobayashi, T. Yasui, *Faraday Discuss*, 2007, **134**, 369-376.

8 J. M. de Souza e Silva, M. Strauss, C. M. Maroneze, E. R. Souza, Y. Gushikem, F. A. Sigoli, I. O. Mazali, *J. Mater. Chem*., 2011, **21**, 15678-15685.

9 Z. P. Li, T. Mori, F. Ye, D. Ou, G. Auchterlonie, J. Zou, J. Drennan, *J. Phys. Chem. C,* 2012, **116**, 5435−5443.

10 Z.P. Li, T. Mori, J. Zou, J. Drennan, *Mat. Res. Bull*., 2013, **48**, 807–812.

11 M. Greenberg, E. Wachtel, I. Lubomirsky, J. Fleig, J. Maier, *Adv. Funct. Mater*., 2006, **16**, 48-52.

12 T. Taniguchi, T. Watanabe, N. Sugiyama, A. K. Subramani, H. Wagata, N. Matsushita, M. Yoshimura, *J. Phys. Chem. C*, 2009,**113**, 19789-19793.

13 G. B. Balazs, R. S. Glass, *Solid State Ionics*, 1995,**76**, 155-162.

14 H. Inaba. H. Tagawa, *Solid State Ionics*, 1996, **83**, 1-16.

15 S. A. Acharya, *J. Power Source*, 2011, **198**, 105-111.

16 Sk. Anirban, A. Dutta, *J. Phys. Chem. Solids*, 2015,**76**, 178-183.

17 S. Sain, S. Patra, S. K. Pradhan, *Mat. Res. Bull*., 2012,**47**, 1062-1072.

18 H. M. Rietveld, *J. Appl. Cryst*., 1969, **2**, 65-71.

19 L. Lutterolti, P. Scardi, P. Maistrelli, *J. Appl. Cryst*., 1992,**25**, 459-462.

20 R. A. Young in: R. A. Young (Ed.), The Rietveld method, Oxford University Press/IUCr, 1996, pp. 1-38.

21 L. B. McCusker, R. B. Von Dreele, D. E. Cox, D. Louer, P. Scardi, *J. Appl. Cryst*., 1999, **32**, 36-50.

22 N. C. Popa, *J. Appl. Cryst*., 1998, **31**, 176-180.

23 S. Gangopadhyay, D. D. Frolov, A. E. Masunov, S. Seal, *J. Alloy. Compd*., 2014, **584**, 199-208.

24 M. Nakayama, M. Martin, *Phys. Chem. Chem. Phys*., 2009, **11**, 3241-3249.

25 S.J. Hong, K.Mehta, A.V. Virkar, *J. Electrochem. Soc.*, 1998, **145**, 638-647.

26 T. Mori, T. Kobayashi, Y. Wang, J. Drennan, T. Nishimura, J.G. Li, and H. Kobayashi, *J. Am. Ceram. Soc*., 2005, **88**, 1981-1984.

27 A.K. Baral, V. Sankaranarayanan, Nanoscale Res. Lett., 2010, **5**, 637-643.

28 L. Vegard, H. Dale, *Zeitschrift Fur Kristallographie*, 1928, **67**, 148-162.

29 D. Pérez-Coll, P. Núñez. J. C. Ruiz-Morales, J, Peña-Martíez, J. R. Frade, *Electrochim. Acta*, 2007, **52**, 2001-2008.

30 S. Omar, E. D. Wachsman. J. C. Nino, *Solid State Ionics*, 2008, **178**, 1890-1897.

31 L. Li, G. Li, Y. Che, W. Su, *Chem. Mater*., 2000, **12**, 2567-2574.

32 D. R. Ou, T. Mori, F. Ye, J. Zou, G. Auchterlonie, J. Drennan, *Phys. Rev. B,*2008, **77**, 024108.

33 Ya-Wen Zhang, R. Si, Chun-Sheng Liao, Chun-Hua Yan, Chao-Xian Xiao, Y. Kou, *J. Phys. Chem. B*, 2003, **107**, 10159-10167.

34 S. L. S. Rao, G. Ramdevudu, Md. Shareefuddin, A. Hameed, M. N. Chary, M. L. Ro, *Int. J. Eng. Sci.Tech.,*2012, **4**, 25-35.

35 E. Wuilloud, B. Delley, W. D. Schneider, Y. Baer, *Phys. Rev. Lett*., 1984, **53**, 202-205.

36 L. Wu, H. J. Wiesmann, A. R. Moodenbaugh, R. F. Klie, Y. Zhu, D. O. Welch, M. Suenaya, *Phys. Rev. B*, 2004, **69**, 125415

37 Gao-Ren Li, Dun-Lin Qu, L. Arurault, Ye-Xiang Tong, *J. Phys. Chem. C*, 2009, **113**, 1235-1241.

38 K. Kuntaiah, P. Sudarsanam, B. M. Reddy, A. Vinu, *RSC Adv*., 2013,**3**, 7953-7962.

39 Z. Wang, Z. Quan, J. Lin, *Inorg. Chem*., 2007, **46**, 5237-5242.

40 C. Sun, H. Li, H. Zhang, Z. Wang, L. Chen, *Nanotechnology*, 2005, **16**, 1454-1463.

41 A. H. Morshed, M. E. Moussa, S. M. Bedair, R. Leonard, S. X. Liu, N. El-Masry, *Appl. Phys. Lett*., 1997,**70**, 1647-1649.

42 M. Sarkar, R. Rajkumar, S. Tripathy, S. Balakumar, *Mater. Res. Bull*, 2012, **47**, 4340-4346.

43 I. Atribak, A. Bueno-L□pez, A. García- García, *J. Catal*., 2008, **259**, 123-132.

44 J. R. McBride, K. C. Hass, B. D. Poindexter, W. H. Weber, *J. Appl. Phys*., 1994, **76**, 2435-2441.

45 E. C. C. Souza, E. N. S. Muccillo*, J. Alloys Compd.,* 2009, **473**, 560-566.

46 T. Taniguchi, T. Watanabe, N. Sugiyama, A. K. Subramani, H. Wagata, N. Matsushita, M. Yoshimura, *J. Phys. Chem. C*, 2009, **113**, 19789-19793.

47 R. O. da Fonseca, A. A. A. da Silva, M. R. M. Signorelli, R. C. Rabelo-Neto, F. B. Noronha, R. C. C. Simões, L. V. Mattos, *J. Braz. Chem. Soc*., 2014, **25**, 2356-2363.

48 A. Nakajima, A. Yoshihara, M. Ishigame, *Phys. Rev. B*, 1994, **50**, 13297-13307.

49 S.F. Wang, C.T. Yeh, Y.R. Wang, Y.C. Wu*, J. Mater. Res. Technol*., 2013, **2**, 141-148.

50 Z.D. Dohčević-Mitrovic, M.J. Šćepanovic, M.U. Grujić-Brojčin, Z.V. Popovic, S.B. Boškovic, B.M. Matovic, M.V. Zinkevich, F. Aldinger, *Solid State Comm.*, 2006, **137**, 387-390.

51 Raghvendra, R. K. Singh, P. Singh, *J. Mater. Sci*., 2014, **49**, 5571–5578.

52 J. C. Dyre, *J. Appl. Phys*., 1988, **64**, 2456-2468.

53 S. Kuharuangrong, *J. Power Sources*, 2007, **171**, 506-510.

54 Y. Wang, T. Mori, J.G. Li, J. Drennan, *J. Eur. Ceram. Soc.*, 2005, **25**, 949-956.

55 B. Roling, A. Happe, K. Funke, M. D. Ingram, *Phys. Rev. Lett*., 1997, **78**, 2160.

56 Raghvendra, P. Singh, R. K. Singh, *J. Alloy Compd*., 2013,**549**, 238-244.

Figure captions:

Fig. 1 (a) XRD patterns of the doped and undoped ceria $Ce_{1-x}Dy_xO_{2-\delta}$ (x=0.00 – 0.50), (b) Shift of (111) peak shift with doping concentration x. The refined XRD patterns obtained from Rietveld analysis for the samples for (c) x = 0.20 and (d) x = 0.50.

Fig. 2 The crystal structure of (a) pure ceria and (b) doped ceria.

Fig. 3 Variation of lattice parameter with the doping concentration x.

Fig. 4 Energy dispersive X-ray analysis (EDAX) for (a) x = 0.00, (b) x = 0.10, (c) x = 0.20 and (d) x = 0.50. The percentage of Dy/Ce values are given in the inset.

Fig. 5 (a) indicates the distribution of nano flakes for the composition x = 0.2. The crystallite size distribution is also shown in the inset of (a). In (b) the lattice plane is shown. The FFT image is also shown in the inset of (b). The simulated lattice pattern is shown in (c). In (d) the atomic model indicates the orientation of the atoms. The gray spheres in (d) indicate the Ce^{4+}/Dy^{3+} atom whereas darker spheres are O^{2-}.

Fig. 6 (a) The UV-VIS absorption spectra for pure and doped ceria $Ce_{1-x}Dy_xO_{2-\delta}$ (x=0.00 – 0.50) and (b) the plot of $(\alpha h\nu)^2$ as a function of photon energy hν for the sample $Ce_{0.8}Dy_{0.2}O_{2-\delta}$.

Fig. 7 Raman spectra of sintered samples $Ce_{1-x}Dy_xO_{2-\delta}$ (x = 0.0-0.5).

Fig. 8(a) The variation of real part $\sigma'(\omega)$ of complex conductivity as a function of frequency at a temperature 525°C of all the samples, (b) The variation of $\sigma(0)$ with the doping concentration at different temperatures and (c) Arrhenius plot of the system $Ce_{1-x}Dy_xO_{2-\delta}$ (x=0.10 – 0.50).

Fig. 9 (a)Scaling of the real part of the ac conductivity $\sigma'(\omega)$ of the complex conductivity spectra $\sigma^*(\omega)$ for $Ce_{0.8}Dy_{0.2}O_{2-\delta}$ at several temperatures and (b)Conductivity master curve for different compositions at temperature 500°C.

Table 1. Rietveld refinement analysis result and theoretical density for the samples $Ce_{1-x}Dy_xO_{2-\delta}$ (x=0.00 – 0.50). The errors after fourth decimal are indicated inside parenthesis.

$Ce_{1-x}Dy_xO_{2-\delta}$ (x=0-0.5)	X = 0.00	X = 0.10	X = 0.15	X = 0.20	X = 0.25	X = 0.30	X = 0.40	X = 0.50
Crystal system	cubic	cubic	cubic	cubic	cubic	cubic	cubic	cubic
Space group	$Fm\bar{3}m$	$Fm\bar{3}m$	$Fm\bar{3}m$	$Fm\bar{3}m$	$Fm\bar{3}m$	$Fm\bar{3}m$	$Fm\bar{3}m$	$Fm\bar{3}m$
Atomic co-ordinate								
Ce(4a)								
(x,y,z)	(0,0,0)	(0,0,0)	(0,0,0)	(0,0,0)	(0,0,0)	(0,0,0)	(0,0,0)	(0,0,0)
Occupancy	0.9989(7)	0.9106(1)	0.8499(5)	0.8039(3)	0.7632(2)	0.7155(1)	0.6265(7)	0.5091(2)
Dy(4a)								
(x,y,z)	---------	(0,0,0)	(0,0,0)	(0,0,0)	(0,0,0)	(0,0,0)	(0,0,0)	(0,0,0)
Occupancy	---------	0.0894(5)	0.1501(3)	0.1961(8)	0.2368(4)	0.2845(4)	0.3735(7)	0.4909(2)
O(8c)								
(x,y,z)	$(\frac{1}{4},\frac{1}{4},\frac{1}{4})$	$(\frac{1}{4},\frac{1}{4},\frac{1}{4})$	$(\frac{1}{4},\frac{1}{4},\frac{1}{4})$	$(\frac{1}{4},\frac{1}{4},\frac{1}{4})$	$(\frac{1}{4},\frac{1}{4},\frac{1}{4})$	$(\frac{1}{4},\frac{1}{4},\frac{1}{4})$	$(\frac{1}{4},\frac{1}{4},\frac{1}{4})$	$(\frac{1}{4},\frac{1}{4},\frac{1}{4})$
Occupancy	0.9859(1)	0.9482(5)	0.9334(8)	0.8898(6)	0.8813(2)	0.8634(1)	0.8176(1)	0.7698(5)
Lattice parameter (Å)	5.3976(9)	5.4019(1)	5.4045(5)	5.4064(4)	4.4085(3)	5.4101(1)	5.4117(8)	5.4138(0)
Particle size (nm)	14.86	21.65	16.67	13.88	13.49	13.78	20.16	21.53
r.m.s. strain	1.25×10^{-5}	8.33×10^{-4}	2.25×10^{-4}	1.25×10^{-5}	7.68×10^{-5}	3.14×10^{-4}	1.25×10^{-4}	1.07×10^{-3}
Ce-O bond length (Å)	2.3372(7)	2.3391(0)	2.3402(4)	2.3410(6)	2.3419(6)	2.3426(5)	2.3433(7)	2.3442(4)
Density (gm/cm^3)	7.268	7.312	7.332	7.354	7.376	7.399	7.453	7.505
R_{wp} (%)	5.42	4.34	5.26	5.79	3.69	3.61	4.34	5.03
R_{exp}(%)	4.63	3.91	4.69	5.03	3.29	3.11	3.67	4.37
GOF	1.17	1.11	1.12	1.15	1.12	1.16	1.18	1.15

Table 2.The values of band gap (E_g) for the samples $Ce_{1-x}Dy_xO_{2-\delta}$ (x=0.00 – 0.50). The errors after third decimal are indicated inside parenthesis.

Samples	Band gap (eV)
CeO_2	2.750(5)
$Ce_{0.9}Dy_{0.1}O_{2-\delta}$	2.714(1)
$Ce_{0.85}Dy_{0.15}O_{2-\delta}$	2.685(4)
$Ce_{0.8}Dy_{0.2}O_{2-\delta}$	2.590(3)
$Ce_{0.75}Dy_{0.25}O_{2-\delta}$	2.529(2)
$Ce_{0.7}Dy_{0.3}O_{2-\delta}$	2.516(1)
$Ce_{0.6}Dy_{0.4}O_{2-\delta}$	2.511(8)
$Ce_{0.5}Dy_{0.5}O_{2-\delta}$	2.471(5)

Table 3. Positions of different Raman bands and intensity ratio of different Raman bands for the samples $Ce_{1-x}Dy_xO_{2-\delta}$ (x=0.00 – 0.50).

Samples	Positions of Raman bands (cm^{-1})			$I_{F_{2g}} / I_{D_1}$	$I_{F_{2g}} / I_{D_2}$	I_{D_1} / I_{D_2}
	F_{2g}	D_1	D_2			
CeO_2	462	-	-	-	-	-
$Ce_{0.9}Dy_{0.1}O_{2-\delta}$	463	552	597	12.81	14.22	1.09
$Ce_{0.8}Dy_{0.2}O_{2-\delta}$	465	558	599	6.00	7.53	2.24
$Ce_{0.7}Dy_{0.3}O_{2-\delta}$	467	563	600	3.13	3.76	1.20
$Ce_{0.6}Dy_{0.4}O_{2-\delta}$	472	571	605	2.01	2.19	1.08
$Ce_{0.5}Dy_{0.5}O_{2-\delta}$	484	576	610	1.51	1.51	1.00

Table 4. The values of activation energy (E_a) and conductivity for the samples $Ce_{1-x}Dy_xO_{2-\delta}$ (x=0.10 – 0.50). The errors after second decimal are indicated inside parenthesis.

Sample	Activation energy (eV)	Conductivity at 550°C ($\Omega^{-1}cm^{-1}$)
$Ce_{0.9}Dy_{0.1}O_{2-\delta}$	1.12(2)	5×10^{-5}
	0.79 [ref: 54]	2×10^{-4}
$Ce_{0.85}Dy_{0.15}O_{2-\delta}$	1.10(9)	3×10^{-4}
	0.86 [ref:15]	7.42×10^{-2}
$Ce_{0.8}Dy_{0.2}O_{2-\delta}$	1.10(5)	5×10^{-4}
	1.16 [ref:27]	1.36×10^{-4}
$Ce_{0.75}Dy_{0.25}O_{2-\delta}$	1.15(8)	3.3×10^{-4}
$Ce_{0.7}Dy_{0.3}O_{2-\delta}$	1.19(8)	2.9×10^{-4}
	1.15 [ref:53]	
$Ce_{0.6}Dy_{0.4}O_{2-\delta}$	1.21(4)	8×10^{-5}
$Ce_{0.5}Dy_{0.5}O_{2-\delta}$	1.46(2)	1×10^{-5}

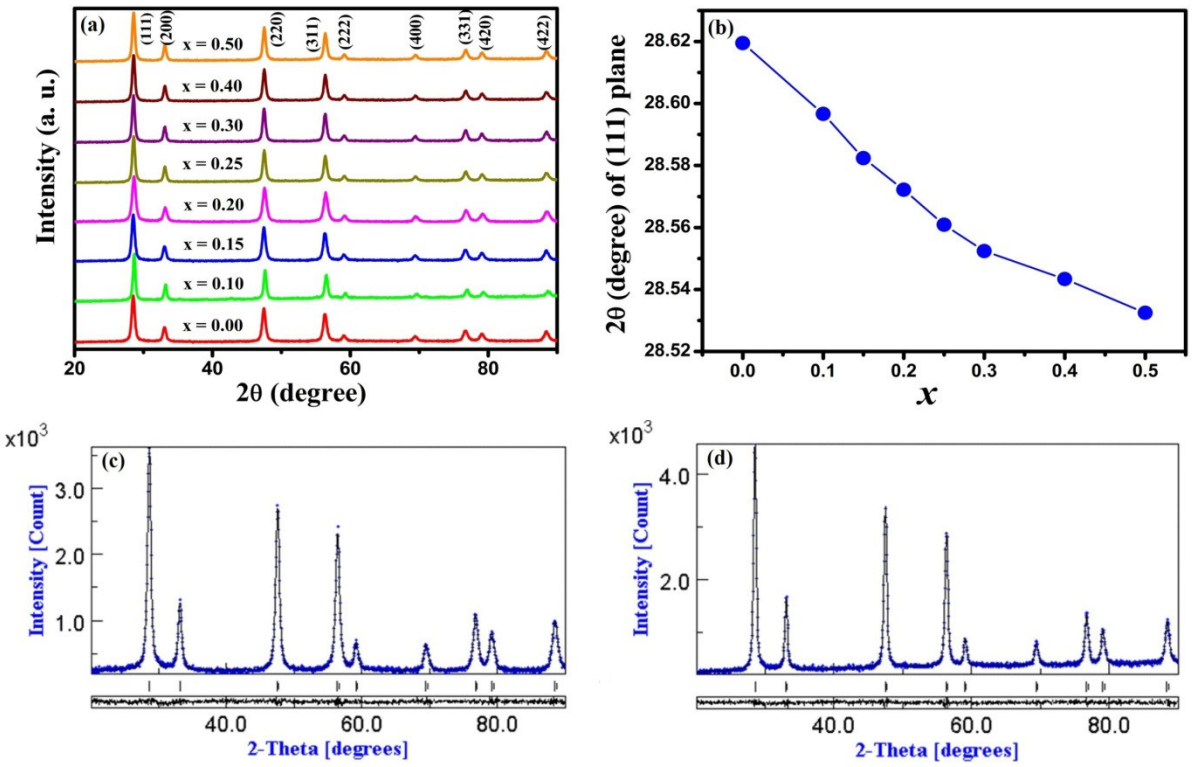

Figure 1

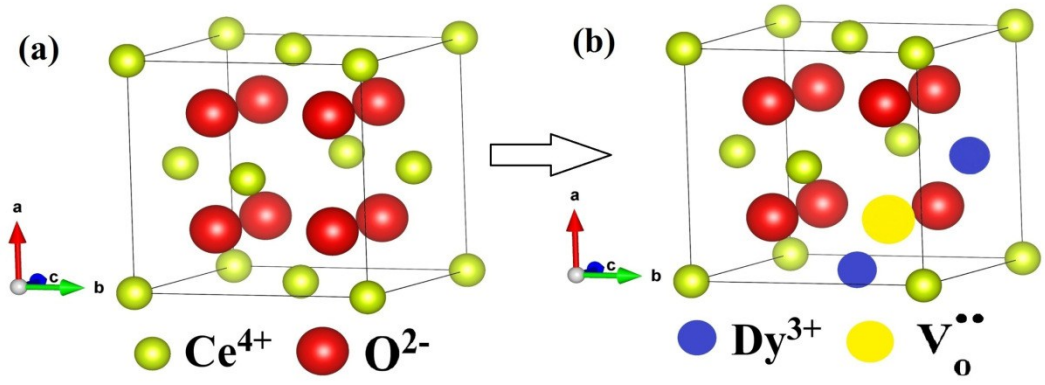

Figure 2

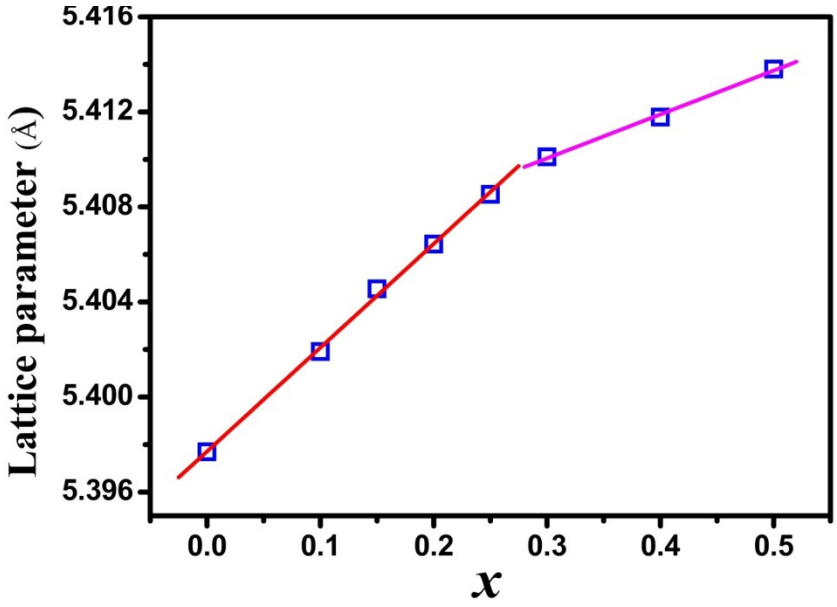

Figure 3

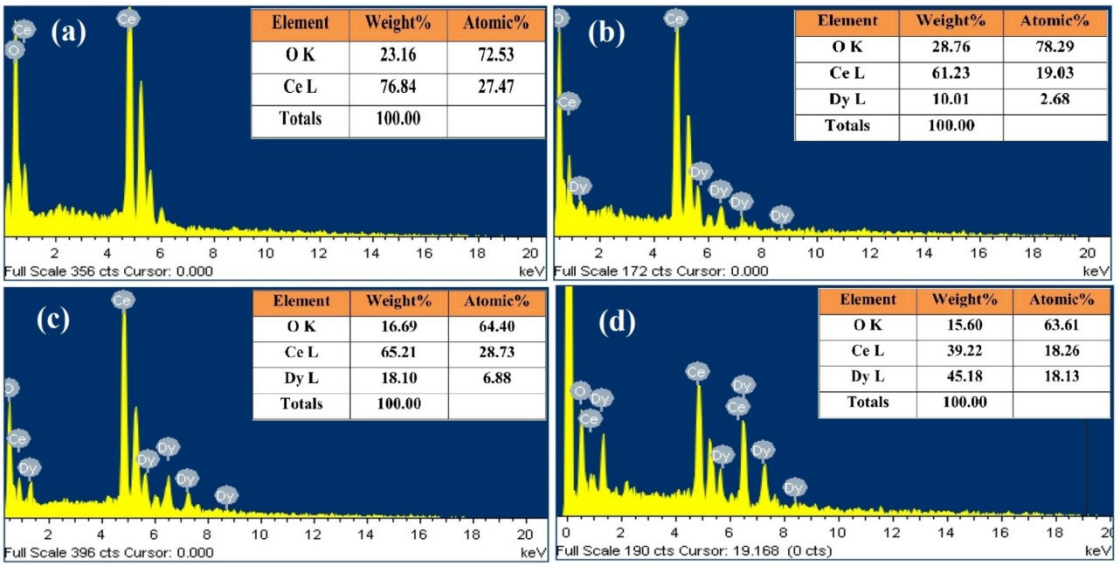

Figure 4

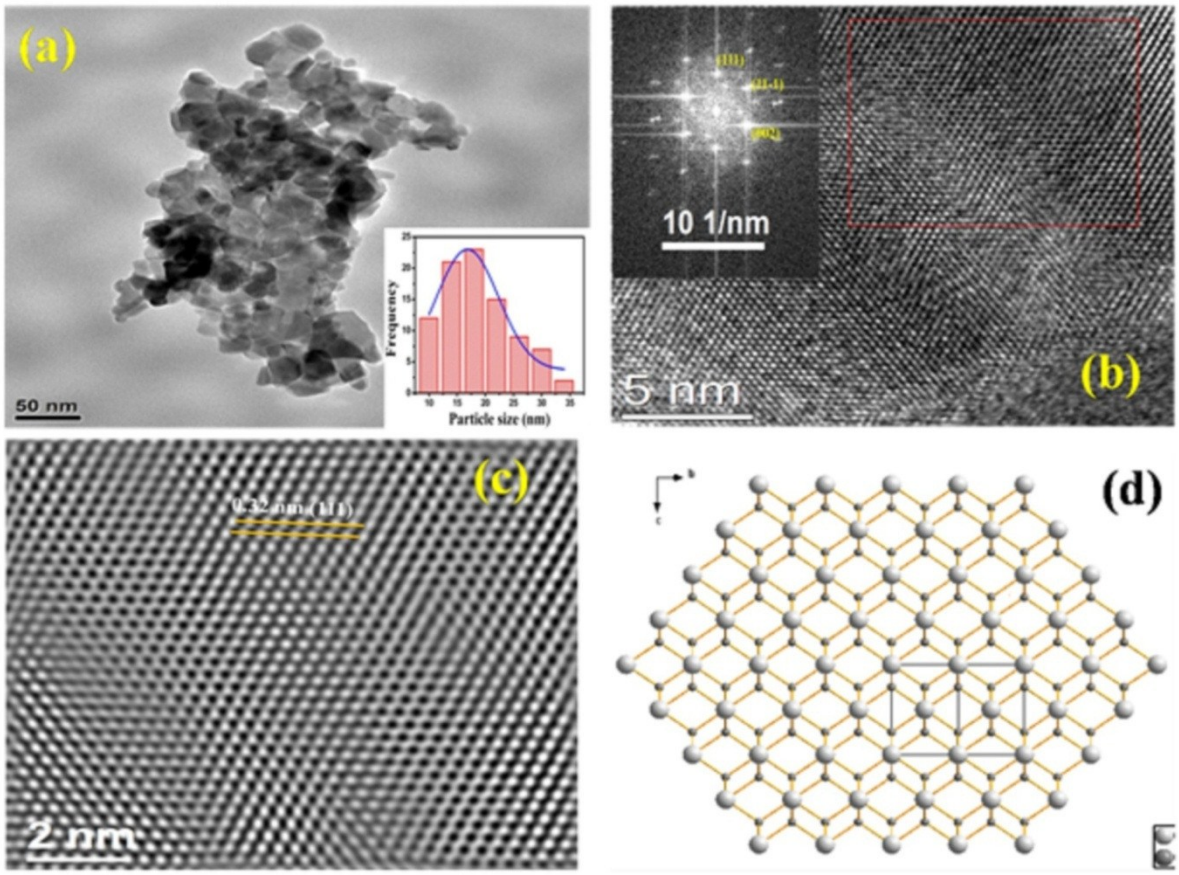

Figure 5

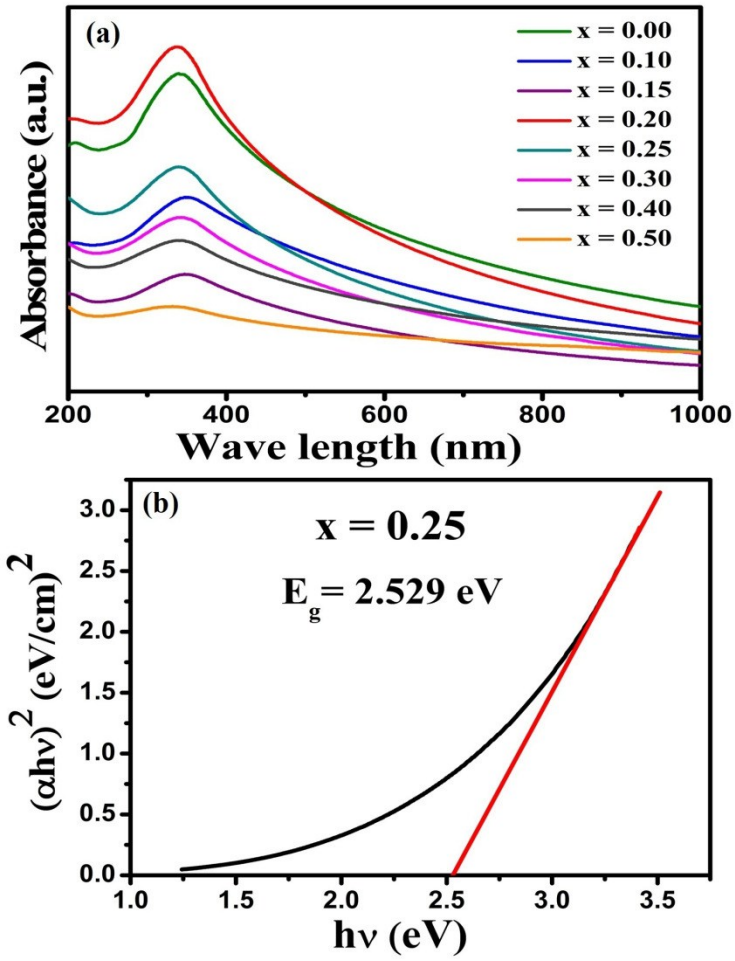

Figure 6

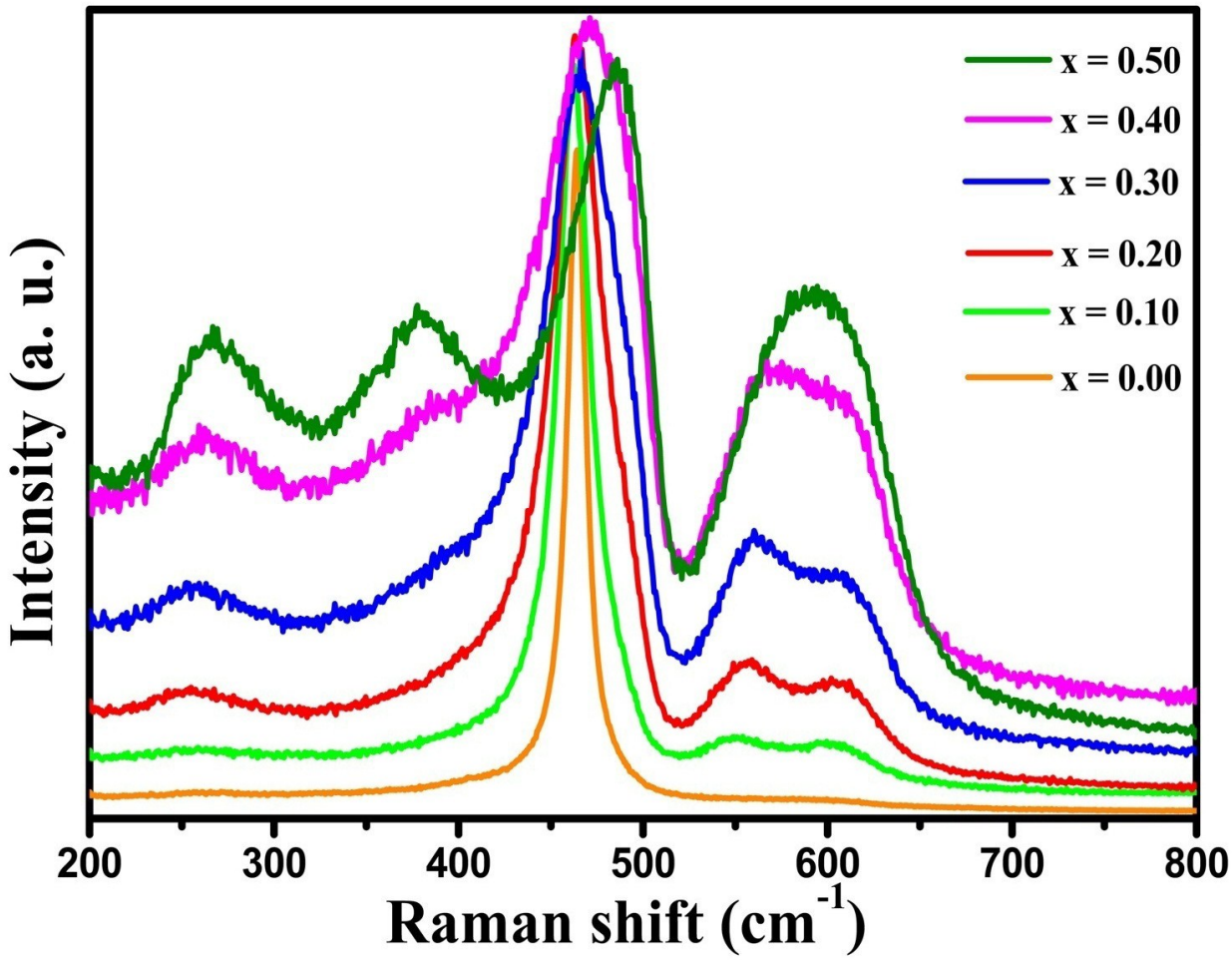

Figure 7

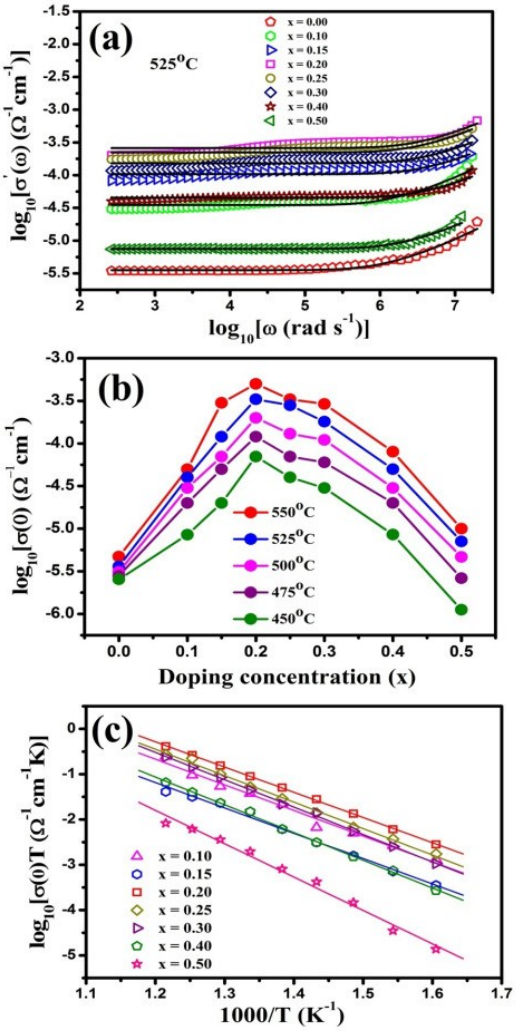

Figure 8

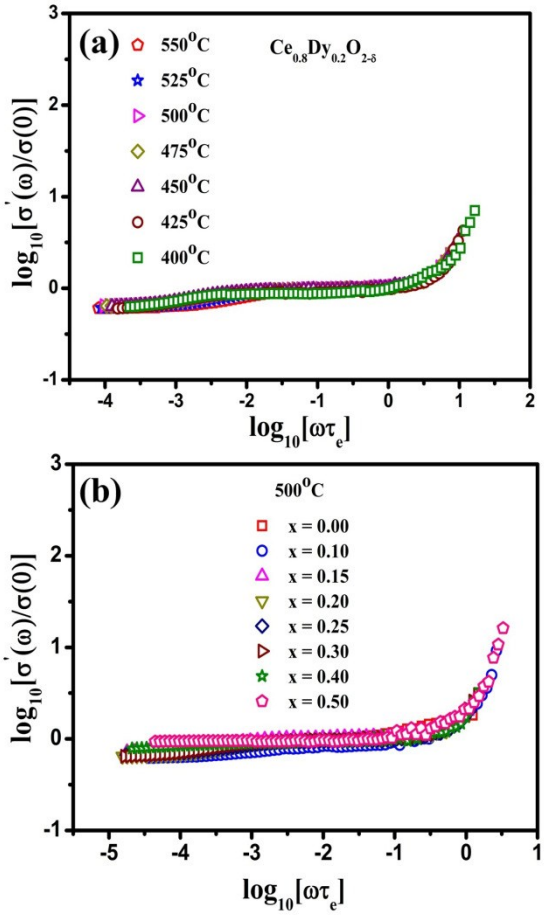

Figure 9